Nanoscale

Accepted Manuscript

This article can be cited before page numbers have been issued, to do this please use: R. Chand, S. Ramalingam and S. Neethirajan, *Nanoscale*, 2018, DOI: 10.1039/C8NR00697K.

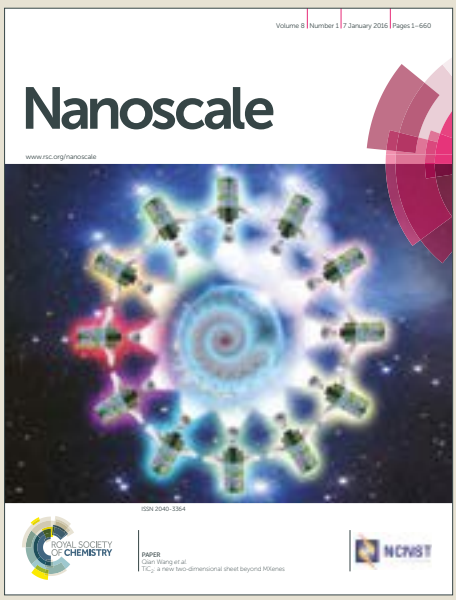

ROYAL SOCIETY OF CHEMISTRY

rsc.li/nanoscale

View Article Online
DOI: 10.1039/C8NR00697K

2D Transition-Metal Dichalcogenide MoS_2 Based Novel Nanocomposite and Nanocarrier for Multiplex miRNAs Detection

Rohit Chand, Saipriya Ramalingam, Suresh Neethirajan*

BioNano Laboratory, School of Engineering, University of Guelph, Guelph, ON, N1G 2W1, Canada

*Corresponding author: sneethir@uoguelph.ca (S. Neethirajan)

View Article Online
DOI: 10.1039/C8NR00697K

Abstract

Nanoscale MoS_2 has attracted extensive attention for sensing due to its superior properties. This study outlines a microfluidic and electrochemical biosensing methodology for the multiplex detection of paratuberculosis-specific miRNAs. Herein, we report the synthesis of MoS_2 nanosheets decorated with copper ferrite ($CuFe_2O_4$) nanoparticles composite and molecular probe immobilized MoS_2 nanosheets as nanocarriers for the electrochemical detection of miRNAs. Paratuberculosis is a bacterial infection of the intestinal tract of dairy cattle, and is a cause of substantial economic and animal losses all over the world. The designed biosensing electrode was modified with synthesized MoS_2-$CuFe_2O_4$ nanocomposites for a highly amplified signal generation. Additionally, selective detection of miRNAs was accomplished by functionalizing the MoS_2 nanosheets with the miRNA-specific biotin-tagged thiolated molecular probe and ferrocene thiol. The presence of target miRNA triggered the opening of molecular probe present on the nanocarriers. The interaction of molecular probe and miRNA resulted in an increase in the electrochemical signal from ferrocene. The optimized microfluidic biosensor was employed to detect a range of miRNA concentrations from the target analyte. Using square wave voltammetric analysis, a detection limit of 0.48 pM was calculated, with a detection range of 1 pM to 1.5 nM. The application of biosensor was also assessed by detecting miRNAs in spiked serum and positive clinical samples. The developed nanomaterial enabled biosensor easily discriminated between the target miRNAs and other interfering molecules. The developed microfluidic biosensor has the potential to be used as a point-of-care, miRNA based diagnostic tool for paratuberculosis in dairy cows.

Keywords: Biosensor, Electrochemical detection, miRNA, MoS_2 nanosheets, Nanocomposite, Paratuberculosis

View Article Online
DOI: 10.1039/C8NR00697K

1. Introduction

Graphene-like two-dimensional (2D) transition metal dichalcogenides (TMDCs) are considered as the most promising nanomaterials for the progression of future electronics.[1] Monolayer TMDCs like MoS_2, WS_2, WSe_2, etc. have shown potential in a myriad of research interests.[2–4] The MoS_2 monolayer is a covalently sandwiched structure of molybdenum atoms between two sulfur atoms, with a thickness of ~0.65 nm. MoS_2 nanosheets have superior electrical, physical, optical and chemical properties; making it an ideal material for developing biosensors.[5,6] A direct band gap of 1.8 eV results in admirably fast heterogeneous electron-transfer capabilities within its atomically thin monolayer, enabling highly sensitive electrical and electrochemical sensing. Additionally, a large surface area of MoS_2 nanosheets can be loaded with several organic and inorganic molecules to develop novel nanocomposites and nanocarriers. Due to these intriguing properties, MoS_2 nanosheets has the potential for innovative applications in sensing of several bio-chemical molecules.

Lithium intercalation exfoliation, liquid exfoliation, and vapor deposition are some of the methods to synthesize mono or few-layered MoS_2 from bulk MoS_2.[7] MoS_2 nanosheets obtained through these routes accompany abundant intrinsic and extrinsic defects such as sulfur vacancies. Although these defects are prime traps of charge carriers, they bestow new opportunities to tailor the physio-chemical properties of MoS_2, which is not feasible in unflawed MoS_2.[8] More commonly, sulfur-containing molecules can be directly substituted with sulfur vacancies, thus opening pathways for functionalized MoS_2 nanosheets.

The electrochemical properties of MoS_2 nanosheets can be further expanded by synthesizing metal nanoparticles (NPs)-decorated MoS_2 nanosheets. Several 2D MoS_2 based nanocomposites like MoS_2-TiO_2, MoS_2-C_3N_4 and MoS_2-Ge have been reported to date.[9–11] Nanocomposites offer superior electronic properties, high surface ratio, catalytic properties,

View Article Online
DOI: 10.1039/C8NR00697K

and biocompatibility. Constituents of nanocomposites retain their individual properties, as well as impart novel properties resulting from their combination.

Paratuberculosis (pTb), or Johne's disease, caused by *Mycobacterium avium* subspecies *paratuberculosis* (MAP) is an infection of the intestinal tract of ruminants.[12] The pTb infection results in diarrhea and wasting, with no cure. Usually, less than five percent of infected ruminants develops clinical signs, while continuously infecting rest of the herd. Death and premature culling of cattle afflicted with pTb is estimated to cost $250 million dollars annually for the dairy industries in the United States.[13] Conventional laboratory testing require a combination of complementary analysis and repeated sampling to diagnose pTb in sub-clinical cattle, making them impractical diagnostic option.[13,14] A point-of-care (POC) diagnostic device for pTb is highly crucial for limiting the transmission of MAP and, in turn, mitigating animal fatality and economic losses.[15] Current biosensor research for pTb detection involves fluorescence, conductance, surface-enhanced Raman scattering, or surface plasmon based immunosensing.[16,17] Recently, an interferon gamma aptasensor was reported for the electrochemical detection of pTb.[18] However, immunosensing of pTb lacks selectivity and diagnostic ability in the sub-clinical stages.

In this study, we designed a microfluidic platform integrated with electrochemical detection for miRNA based new-generation diagnostic assay of pTb. Recently, miRNAs have been shown to have significant potential as novel biomarkers for the detection of pTb.[19–21] The sensitive and selective quantification of miRNA is highly challenging. Modern biosensing techniques like fluorescence, surface plasmon resonance, electrochemistry, rolling-circle amplification, etc. have also been reported to overcome the troubles of conventional assays.[22–24] Electrochemical biosensors are advantageous due to high selectivity, sensitivity, and rapid analysis. These biosensors are easy to miniaturize, cost-effective, and label-free.[25]

View Article Online
DOI: 10.1039/C8NR00697K

In summary, we propose a proof-of-concept microfluidic and electrochemical-based multiplexed miRNAs biosensor for the rapid, sensitive and selective diagnosis of pTb. The microfluidic platform integrates sample processing zones and a novel MoS_2 nanosheets and copper ferrite nanoparticles ($CuFe_2O_4$ NPs) composite modified electrode. The Cu based NPs are known to have superior catalytic activity thereby enhancing the electrochemical reactions.[26] The selective detection of miRNAs was accomplished by employing biotin-tagged thiolated molecular probe and ferrocene thiol functionalized MoS_2 nanosheets as novel nanocarrier. In the presence of target miRNAs, the hybridization of miRNAs with the loop region resulted in the opening of molecular probe. The biotin end of the molecular probe then linked with the streptavidin-coated magnetic microbeads (Strp-MMBs) present in the reaction mixture. The nanocarriers and Strp-MMBs cluster were accumulated onto the modified electrodes using an external magnet. The MoS_2 nanosheets as nanocarrier enhanced the sensitivity and selectivity of miRNAs detection by serving as a matrix for higher loading of molecular probe and ferrocene reporter. The developed nanocomposite, modified electrode, nanocarriers, and biosensing strategy were characterized using several spectroscopic, microscopic, and electrochemical techniques. Developed biosensing microfluidic platform has the potential for application in POC detection of miRNAs based pTb diagnosis in the clinical samples.

2. Materials and methods

2.1. Materials

N-methyl-2-pyrrolidone (NMP), molybdenum disulfide (MoS_2), copper ferrite nanopowder ($CuFe_2O_4$ NPs, size $\leq$ 100 nm), (3-mercaptopropyl) trimethoxysilane (MPTS), tris-(hydroxymethyl) aminomethane (Tris), ethylenediaminetetraacetic acid (EDTA), tris-(2-carboxyethyl) phosphine hydrochloride (TCEP), 2-aminobenzylamine (ABA), 6-(ferrocenyl)

View Article Online
DOI: 10.1039/C8NR00697K

hexanethiol (FcSH), potassium ferricyanide ($K_3[Fe(CN)_6]$), and potassium ferrocyanide ($K_4[Fe(CN)_6]$) of analytical grade were purchased from Sigma-Aldrich (Oakville, ON, Canada) and used without further purification. Streptavidin-coated magnetic microbeads (Strp-MMBs) were obtained from New England Biolabs Inc (Whitby, ON, Canada). The miRNAs and their respective molecular probes were synthesized by Integrated DNA Technologies (Coralville, IA, USA). The molecular probes were tagged with biotin at 5′-terminal and thiolated at 3′-terminal. The sequence of each pTb specific miRNA and the molecular probe is tabulated in Table S1 and Table S2. Milli-Q water (18.2 MΩ, DI water) was used throughout the experiments. The screen-printed carbon electrodes (SPCEs, model OHT-000) used in this study were purchased from Orion High Technologies (Madrid, Spain). The working (4 mm diameter) and the counter electrode were made of carbon, whereas the reference electrode was made of silver/silver chloride. A High Pure miRNA Isolation Kit (Roche Diagnostics, QC, Canada) was used to extract total miRNA from pTb positive blood samples.

2.2. Synthesis of MoS_2-$CuFe_2O_4$ nanocomposites

The decoration of MoS_2 nanosheets with $CuFe_2O_4$ NPs was based on the thiol chemistry between MoS_2 and MPTS and silane chemistry between $CuFe_2O_4$ NPs and MPTS. The synthesis process of the MoS_2-$CuFe_2O_4$ nanocomposites is schematically illustrated in Figure 1(A). The exfoliated MoS_2 nanosheets were first prepared by ultra-sonicating 1 mg/mL MoS_2 powder in NMP. The dispersion was centrifuged at 4000 rpm and the clear fractions were subsequently used for further studies. For the synthesis of MoS_2-$CuFe_2O_4$ nanocomposites, the exfoliated MoS_2 nanosheets were immediately mixed with MPTS (1% final concentration) and an ethanolic solution of $CuFe_2O_4$ NPs at a volume ratio of 1:1. The concentration of $CuFe_2O_4$ NPs was varied from 0.5 mg/mL to 2 mg/mL. The mixtures were

View Article Online
DOI: 10.1039/C8NR00697K

kept in dark and under stirring for overnight at 100 °C. The obtained MoS_2-$CuFe_2O_4$ nanocomposites were centrifuged to eliminate unused reactants and re-dispersed in DI water. The final nanocomposites were characterized using microscopic and spectroscopic techniques.

2.3. Modification of electrode with MoS_2-$CuFe_2O_4$ nanocomposites

An electrochemical co-deposition technique was adopted to modify SPCEs and achieve robust film stability. The MoS_2-$CuFe_2O_4$ nanocomposites were confined on the electrode while electro-polymerizing ABA homopolymer. 100 mM ABA monomer in 200 mM sulfuric acid was mixed with MoS_2-$CuFe_2O_4$ nanocomposites in 1:1 volume ratio. The ABA and nanocomposites mixture was firstly dropped onto the SPCE surface and electro-polymerized through cyclic voltammetry. The nanocomposites film was grown on the carbon electrode with a potential from -0.2V to 1.2V for 15 cycles at a scan rate of 20 mV/s. The nanocomposites film was thoroughly rinsed with DI water and dried for further studies.

2.4. Functionalization of MoS_2 nanosheets with molecular probe and reporter

The exfoliated MoS_2 nanosheets were first prepared by ultra-sonicating 1 mg/mL MoS_2 powder in NMP. The dispersion was centrifuged at 4000 rpm and the clear fractions were subsequently used for further functionalization. The exfoliated MoS_2 nanosheets were washed repeatedly with ethanol followed by re-dispersion in 1X Tris-EDTA buffer (TE buffer). Functionalization of the MoS_2 nanosheets was carried out by mixing nanosheets with 2 μM molecular probe and 0.2 mM FcSH (electrochemical reporter).[27] The mixtures were kept under stirring, in dark for overnight. This was followed by centrifuging the mixture to remove non-immobilized molecular probe and FcSH. The obtained functionalized MoS_2 nanosheets (nanocarriers) were re-dispersed in TE buffer. A total of four nanocarriers were

View Article Online
DOI: 10.1039/C8NR00697K

synthesized and termed as MoS_2-MP_{7857}, MoS_2-MP_{378}, MoS_2-MP_{92}, and MoS_2-MP_{205}, respectively for each miRNA.

2.5. Microfluidic platform fabrication

The design of SPCE integrated all- polydimethylsiloxane (PDMS) based 3D microfluidic platform is shown in Figure 1(C). The microfluidic platforms were fabricated using the standard lithography technique. A silicon and SU-8 based master mold was fabricated for making PDMS engraved microchannels.[25] The microfluidic platform consisted of different zones for reaction and sensing. 3D microfluidic network assisted in improved flow and operation of the microfluidic platform. The height and the width of each microchannel was 100 μm and 200 μm, respectively. The top PDMS layer contained branched inlet for the miRNA sample. The middle layer contained four mixing zones, four incubation zones, four sensing zones, and outlets. The mixing zones housed numerous barriers to enhance the mixing of reagents. The bottom layer of PDMS was molded containing the groove for the SPCE. The three PDMS layers and SPCEs were aligned under an optical microscope and irreversibly bonded, after oxygen plasma treatment. A thin layer of epoxy glue was also carefully smeared around the electrode for improved adhesion.

2.6. Electrochemical detection of miRNAs

The one-step and label-free detection of miRNAs were based on MoS_2-MP and miRNA interaction as illustrated in Figure 1(B and C). Varied concentrations of miRNA (20 μL) or spiked serum sample prepared in 1X TE buffer was injected into sensing zone through the inlet (I_1, Figure 1(C)) of the microfluidic platform. Four different mixtures containing each of MoS_2-MP and Strp-MMBs were injected through $I_{2\text{-}5}$. The miRNA sample and respective MoS_2-MP mixtures underwent thorough mixing in the mixing zones and then passed through the incubation zone. The selective molecular probes immobilized on the MoS_2 nanosheets

View Article Online
DOI: 10.1039/C8NR00697K

captured the miRNAs. The magnets placed under the electrodes in sensing zone trapped all the MoS_2-MP and Strp-MMBs complex, while allowing all unreacted MoS_2-MP exit through the outlets (O_{1-4}). All the studies involving optimization and single miRNA detection was performed in microfluidic platform shown in Figure S1.

The miRNA analysis was enhanced by optimizing the amount of MoS_2-MP and Strp-MMBs. The interaction time of miRNA and MoS_2-MP was measured by changing the flow-rate of mixture ranging from 25 µL/hr to 200 µL/hr. The optimized microfluidic miRNA biosensor was tested for its electrochemical response to varying concentrations of miRNA. Multiplexed miRNAs detection was performed in spiked serum and pTb positive bovine blood samples to investigate the selectivity and applicability of the proposed sensor.

All the electrochemical measurements were carried out in triplicates, with the PalmSens4 potentiostat (Palmsens, Houten, Netherlands). Cyclic voltammetry (CV) and square wave voltammetry (SWV) were recorded in 1X PBS. The CV measurements were performed in the potential range from −0.8 to 0.8 V at a scan rate of 100 mV/sec. The SWV measurements were performed in the potential region from 0 to 0.7 V at a step potential of 10 mV, amplitude of 50 mV and frequency of 2 Hz. A solution 5 mM $K_3[Fe(CN)_6]$ and 5 mM $K_4[Fe(CN)_6]$ in 1X PBS was used for CV, wherever applicable. The SPCE on the integrated microfluidic platform was directly inserted into the electrode holder for electrochemical analysis.

2.7. Validation experiments using ELISA and RT-PCR

The blood and fecal samples obtained from the pTb-infected cows across the Ontario were first validated using the commercial Idexx MAP Ab Test (IDEXX Laboratories Inc, ME, USA) and the VetAlert™ Johne's Real-Time PCR kit (Tetracore, MD, USA),

View Article Online
DOI: 10.1039/C8NR00697K

respectively. All the sample extraction and analysis were performed as per the manufacturer's instructions.

3. Results and discussion

3.1. Characterization of MoS_2-$CuFe_2O_4$ nanocomposites

The MoS_2-$CuFe_2O_4$ nanocomposites were synthesized by a simple one-step strategy using MPTS as a chemical linker (Figure 1(A)). The exfoliation of MoS_2 leads to deformation of crystal structure and formation of numerous sulfur vacancies in the peripheral and internal edges of the nanosheets. These sulfur vacancies possess high affinity towards thiol molecules. Therefore, the mercapto- groups in MPTS substituted these vacancies; simultaneously silane- groups covalently bonded to the $CuFe_2O_4$ NPs. The exfoliated MoS_2 nanosheets and MoS_2-$CuFe_2O_4$ nanocomposites were systematically characterized by several spectroscopic and microscopic techniques. The UV-visible spectroscopic analysis of pristine MoS_2 nanosheets is shown in Figure 2(A), revealing characteristic absorbance peaks of 2D MoS_2 located at 675 and 612 nm due to band gap energies of 1.85 eV and 2.03 eV, respectively. The transition of electrons to the conduction band from the valence band in MoS_2 nanosheets also exhibited one broad characteristic peak at 400–450 nm.[4] UV-visible spectroscopy of MoS_2-$CuFe_2O_4$ nanocomposites is also shown in Figure 2(A). It can be seen that the representative peak of MoS_2 nanosheets diminished due to the coverage of surface with $CuFe_2O_4$ NPs and a collective spectrum was displayed by the nanocomposites.

Raman spectroscopy (Figure 2(B)) was performed to confirm the presence of exfoliated MoS_2 nanosheets, as well as MoS_2-$CuFe_2O_4$ nanocomposites. It is well reported that the Raman spectrum of bulk MoS_2 displays two main vibrational peak, the in-plane E^1_{2g} at ~383 cm^{-1} and the out-of-plane A_{1g} at ~408 cm^{-1}.[28] As shown in Figure 2(B), after the exfoliation, the Raman spectra resulted in red-shift for E^1_{2g} peak and blue-shift for A_{1g}, which is

View Article Online
DOI: 10.1039/C8NR00697K

distinctive of the 2D MoS_2 nanosheets. Consequently, the E^1_{2g} and A_{1g} modes in MoS_2-$CuFe_2O_4$ nanocomposites shifted minimally compared with the pristine MoS_2 nanosheets, signifying phonon confinement and increase in disorderness on the MoS_2 surface. An additional peak at ~690 cm^{-1} corresponding to the A_{1g} vibration of FeO bond in the tetrahedral FeO_6 groups of $CuFe_2O_4$ appeared in the Raman spectra of MoS_2-$CuFe_2O_4$ nanocomposites. Figure 2(C) shows the X-ray diffraction (XRD) patterns of MoS_2-$CuFe_2O_4$ nanocomposites. The XRD pattern showed the distinguishing peak of 2H-MoS_2 nanosheets at ~14.50°A (002), indexed as the hexagonal phase of MoS_2 (PDF 00-037-1492).[29] Additional peaks corresponding to cuprospinel $CuFe_2O_4$ NPs at ~40°A were also indexed (PDF 04-007-5165).[30] These data indicate the successful synthesis and good stability of MoS_2-$CuFe_2O_4$ nanocomposites.

The morphologies of pristine MoS_2 nanosheets and MoS_2-$CuFe_2O_4$ nanocomposites are shown in Figure S2. The TEM image in Figure S2(A) reveals the well-distributed sheet-like morphology of exfoliated MoS_2. In the Figure S2(B), high loading of $CuFe_2O_4$ NPs can be seen decorated on the surface of MoS_2 nanosheets. The dark spots correspond to $CuFe_2O_4$ NPs, proving the successful formation of the nanocomposites. The nanocomposites aggregated during the analysis due to the strong magnetic attraction between them.

3.2. Characterization of electrode modification

The electro-polymerization of conducting polymer is advantageous, offering precise control and stability of the resulting layer. The MoS_2-$CuFe_2O_4$ nanocomposites were co-polymerized on electrode surface during the electro-polymerization of amine groups present in ABA. To verify this, we first performed the scanning electrode microscopy (SEM), energy-dispersive X-ray (EDX), and elemental mapping of the electrode surface. The SEM micrograph in Figure 3(A) confirms the modification of electrode with nanocomposites. The

View Article Online
DOI: 10.1039/C8NR00697K

SEM imaging studies indicate a uniform coverage of MoS_2-$CuFe_2O_4$ nanocomposites within the electro-polymerized layer on the electrode surface. The EDX analysis (Figure S3) along with elemental mapping (Figure 3(B)) of the electrode shows the respective peaks of MoS_2 (Mo and S), $CuFe_2O_4$ (Cu and Fe), and MPTS (Si). The presence of the representative peak is a good indication of the successful synthesis of the desired nanocomposites and electrode modification.

The modification of SPCE with different MoS_2-$CuFe_2O_4$ nanocomposites and its electrochemical behavior were validated by cyclic voltammetry (CV). The CV was performed in presence of 5 mM potassium ferricyanide/ferrocyanide ($[Fe(CN)_6]^{3-/4-}$) redox couple prepared in 1X PBS. The CVs at bare carbon and nanocomposites modified electrodes are shown in Figure 3(C). The redox probe $[Fe(CN)_6]^{3-/4-}$ revealed reversible CVs at the SPCEs. The electro-polymerization of nanocomposites on SPCE led to a significant amplification of the current signal from $[Fe(CN)_6]^{3-/4-}$. A successive growth in the peak current is seen with the increasing concentration of $CuFe_2O_4$ NPs in the nanocomposites. The highest and a 200% increment in signal was obtained from the SPCE with MoS_2-$CuFe_2O_4$ (2 mg/mL) nanocomposites. It is believed that higher content of Cu magnified the electro-catalytic activity and conductivity of the nanocomposites. However, further increasing the amount of $CuFe_2O_4$ NPs reduced the signal due to complete masking of the MoS_2 nanosheets (data not shown). Therefore, MoS_2-$CuFe_2O_4$ nanocomposites with a $CuFe_2O_4$ content of 2 mg/mL was used for further studies.

3.3. Characterization of functionalized MoS_2 based nanocarriers

The MoS_2 nanosheets provided a platform for the immobilization of biotin-tagged molecular probe and FcSH. The Fourier-transform infrared spectroscopy (FTIR) spectra of the pristine MoS_2 nanosheets (Figure 4) exhibited the characteristic signals for out-plane

View Article Online
DOI: 10.1039/C8NR00697K

vibration of S atoms (S-S) at ~800 cm^{-1}. The peak for S-O stretching in MoS_2 nanosheets appeared at 1100 cm^{-1}. The signals in the regions of 1720 cm^{-1} in the FTIR spectrum of MoS_2-MP were due to C=O stretching vibrations of the immobilized molecular probe. The peak at 1250 cm^{-1} is attributed to the PO^{2-} group of the DNA bases. The presence of multiple C-H stretching peaks at 3000 cm^{-1}, 1400 $cm^{-1,}$ and 1300 cm^{-1} also signifies attachment of molecular probe and hexane

chain of FcSH. This test verified the functionalization of MoS_2 nanosheets to create the designed nanocarriers for miRNA detection.

3.4. Optimization of electrochemical miRNA sensor

In order to maximize the sensing of miRNAs, experimental conditions such as the MoS_2-MP concentration, Strp-MMBs concentration, and the microfluidic flow-rate of mixtures were studied. The varied volume ratio of miRNA with nanocarrier was reacted to standardize the sensitivity of the analysis. Sensitivity was tested with $miRNA_{205}$ and MoS_2-MP_{205} volume ratio of 1:0.5, 1:1, 1:1.5, 1:2, and 1:4. These experiments were conducted by incubating $miRNA_{205}$, MoS_2-MP_{205}, and Strp-MMBs in a microfuge tube. The MoS_2-MP_{205} linked Strp-MMBs were collected using a magnet and the resulting current signal arising from the immobilized ferrocene was measured. As shown in Figure 5(A), it was found that the current increased with the increasing amount of nanocarrier, reaching a saturation at a ratio of 1:2. A low signal was obtained at a lower amount of nanocarrier due to exhaustion of free hybridization site for miRNA. Therefore, to achieve high assay sensitivity, all of the following analyses were performed using 1:2 volume ratio of miRNAs and nanocarriers.

Several experiments were performed to determine the optimal concentration of Strp-MMBs in order to efficiently collect the target miRNA hybridized MoS_2-MP. Strp-MMBs with a varied concentration range of 25 μg/mL to 500 μg/mL were incubated with $miRNA_{205}$

View Article Online
DOI: 10.1039/C8NR00697K

and MoS_2-MP_{205} in a microfuge tube. After aggregating the MoS_2-MP_{205} and Strp-MMBs cluster, the resulting current signal was measured. Upon SWV study, an increasing current for decreasing Strp-MMBs concentration was observed (Figure 5(B)). The maximum current for miRNA was obtained with a concentration of 50 μg/mL, beyond which no further increase was obtained. A higher signal with lower Strp-MMBs concentration was achieved presumably due to condensed aggregation of linked MoS_2-MP_{205} over the electrode. However, 100 μg/mL of Strp-MMBs was used for further biosensing.

The microfluidic flow-rate was optimized to achieve better mixing and maximum sensitivity within the shortest period. To decide the flow-rate, $miRNA_{205}$ from one inlet and a mixture of MoS_2-MP_{205} and Strp-MMBs from the other inlet was pumped at a different speed. The flow-rate ranged from 200 μL/hr to 25 μL/hr. The variation of the electrochemical signals during SWV after the sample and nanocarriers interaction were recorded. A faster flow-rate leads to incomplete interaction of miRNA with the nanocarriers, thus resulting in lower sensitivity. Based on SWV analysis (Figure 5(C)), the signal increased significantly as the flow-rate decreased up to 50 μL/hr. However, the signal enhanced negligibly at a flow-rate of 25 μL/hr, suggesting that the interaction of miRNA was saturated. Therefore, 50 μL/hr was chosen as the optimum flow-rate.

3.5. Electro-analytical investigation of microfluidic miRNA sensor

By integrating the exceptional properties of MoS_2 nanosheets and metal nanoparticles, a facile electrochemical miRNAs sensor was realized. The detection mechanism behind the miRNA detection for pTb diagnosis is illustrated in Figure 1. The specific interaction of molecular probe immobilized on the MoS_2 nanosheets with miRNA resulted in a Strp-MMBs linked nanocarrier cluster. The electrochemical signal of the electrode increased due to the presence of FcSH on the MoS_2 nanosheets. Under the optimized conditions, $miRNA_{205}$

View Article Online
DOI: 10.1039/C8NR00697K

detection was performed on the microfluidic platform illustrated in Figure S1. Figure 6(A) represents the square wave voltammograms of microfluidic miRNA sensor studied with various concentrations (1 pM – 1.5 nM) of $miRNA_{205}$. An inherent cathodic peak current (Epa = 0.32 V) response from ferrocene immobilized on the nanocarriers in the presence of miRNA was exhibited. The detection of 1.5 nM $miRNA_{205}$ produced the highest signal, signifying a high proportion of nanocarriers and Strp-MMBs cluster. Voltammetry in the absence of miRNA produced no significant signal after the microfluidic operation. The sequential detection of different concentrations of $miRNA_{205}$ distinctly increased the signal as the concentration increased. The change in the signal with respect to varying concentration of $miRNA_{205}$ is also summarized in Figure 6(B). The data points denote an average current signal from $miRNA_{205}$ detection in triplicate (n=3) after baseline correction with standard deviation as error bars. The biosensor showed stable performance, and a linear response curve for miRNA detection was seen (R^2= 0.97). The device showed a detection limit of 0.48 pM for miRNA based on S/N=3 calculation. The analytical performance of this work is compared with previously reported literature, and is summarized in Table S3.

The specificity of this sensing methodology was verified using a non-complementary molecular probe. The attempted detection of $miRNA_{205}$ in presence of MoS_2-MP_{7857} produced no considerable electrochemical signal (Figure 6C). This implies that the molecular probe did not open-up, thus confirming the detection specificity of microfluidic miRNAs sensor. For samples without Strp-MMBs, the miRNA hybridized nanocarriers could not be aggregated, as a result, an insignificant electrochemical signal was obtained (Figure 6C).

3.6. Multiplex detection of miRNAs in biological fluids

During pTb, a number of miRNAs are up-regulated or down-regulated, therefore the multiplex analysis of miRNAs is crucial to provide an expression profile. Therefore, the

View Article Online
DOI: 10.1039/C8NR00697K

simultaneous detection of four miRNAs on the microfluidic platform was performed by spiking the serum with the mixture of target miRNAs. The analysis was performed under optimized conditions, on the microfluidic platform illustrated in Figure 1(C). Table 1 summarizes the analysis of miRNAs spiked in the serum. Marginally higher signals were obtained possibly due to the interference of unknown molecules present in the serum. However, the analysis showed good recoveries of the spiked miRNAs with an average error margin of 2–5%. The results clearly exhibit the applicability of the developed MoS_2 nanosheets and microfluidic based electrochemical miRNAs sensor for the simultaneous detection of several miRNAs through different MoS_2-MP.

The practical application and validation of the proposed multiplexed miRNAs sensor for the diagnosis of pTb in the clinical sample was also performed. For this purpose, we tested blood samples obtained from five different bovines. The extracted total miRNAs were analyzed by the proposed technique, as described in the earlier sections. Blood and fecal samples were cross-examined for the confirmation of pTb using ELISA and RT-PCR. Table 2 summarizes the analysis of clinical samples using all the techniques. The electrochemical analysis of blood confirmed the presence or absence of each miRNA. The concentration of respective miRNA in blood varies with the stage of MAP infection and the age of bovine. The clinical stage of pTb in bovines was unknown due to naturally acquired infection. Nevertheless, a good agreement of the positive samples documented by the proposed electrochemical sensor with those of ELISA and RT-PCR was achieved. As evident from the comparative results, our work can be successfully applied for the point-of-care detection of miRNAs in clinical samples for pTb diagnosis.

4. Conclusions

View Article Online
DOI: 10.1039/C8NR00697K

This study reports the synthesis of MoS_2 based nanocomposite and nanocarrier for biosensing application. As a proof-of-concept, a microfluidic platform for the electrochemical detection of miRNA using nanoscale MoS_2 is demonstrated. MoS_2-$CuFe_2O_4$ nanocomposites were successfully synthesized and electro-polymerized on the working electrode for signal amplification. Similarly, MoS_2 nanosheets provided a high surface area for the immobilization of molecular probes and ferrocene thiol. MoS_2 based nanocarriers aided in increased selectivity for miRNA sensing and signal generation. The one-step multiplex detection of four pTb specific miRNAs was accomplished using the proposed microfluidic platform. SWV studies revealed a detection limit of 0.48 pM for $miRNA_{205}$. The sensor could also detect miRNA with high sensitivity and selectivity in the spiked serum and pTb positive bovine clinical samples. Rapid, on-site detection of pTb is a major concern for veterinarians. The proposed electrochemical-based biosensor could be further developed as a POC device for pTb diagnosis.

Conflicts of interest

The authors declare no conflicts of interest.

View Article Online
DOI: 10.1039/C8NR00697K

References

1 M. Samadi, N. Sarikhani, M. Zirak, H. Zhang, H.-L. Zhang and A. Z. Moshfegh, *Nanoscale Horiz.*, 2018, **3**, 90-204.

2 S. Manzeli, D. Ovchinnikov, D. Pasquier, O. V. Yazyev and A. Kis, *Nat. Rev. Mater.*, 2017, **2**, 17033.

3 G. Zhang, H. Liu, J. Qu and J. Li, *Energy Environ. Sci.*, 2016, **9**, 1190–1209.

4 S. K. Tuteja, T. Duffield and S. Neethirajan, *Nanoscale*, 2017, **9**, 10886–10896.

5 M. Chhowalla, H. S. Shin, G. Eda, L. J. Li, K. P. Loh and H. Zhang, *Nat. Chem.*, 2013, **5**, 263–275.

6 S. K. Tuteja and S. Neethirajan, *Chem. Commun.*, 2017, **53**, 10002–10005.

7 I. Song, C. Park and H. C. Choi, *RSC Adv.*, 2015, **5**, 7495–7514.

8 D. M. Sim, M. Kim, S. Yim, M. J. Choi, J. Choi, S. Yoo and Y. S. Jung, *ACS Nano*, 2015, **9**, 12115–12123.

9 Q. Wang, P. Yu, L. Bai, R. Bao, N. Wang, C. Cheng, Z. Liu, M. Yang, W. Yang and Z. Guo, *Nanoscale*, 2017, **9**, 18194–18201.

10 M.-H. Hsieh, G.-A. Li, W.-C. Chang and H.-Y. Tuan, *J. Mater. Chem. A*, 2017, **5**, 4114–4121.

11 X. Qian, J. Ding, J. Zhang, Y. Zhang, Y. Wang, E. Kan, X. Wang and J. Zhu, *Nanoscale*, 2018, **10**, 1766-1773.

12 R. W. Sweeney, *Vet. Clin. North Am. Food Anim. Pract.*, 1996, **12**, 305–312.

13 A. Tiwari, J. A. VanLeeuwen, S. L. B. McKenna, G. P. Keefe and H. W. Barkema, *Can. Vet. J.*, 2006, **47**, 874–882.

14 L. E. Britton, J. P. Cassidy, J. O'Donovan, S. V. Gordon and B. Markey, *Vet. J.*, 2016, **209**, 32–39.

15 R. Chand, Y. L. Wang, D. Kelton and S. Neethirajan, *Sens. Actuat. B*, 2018, **261**, 31-37.

View Article Online
DOI: 10.1039/C8NR00697K

16 C. Okafor, D. Grooms, E. Alocilja and S. Bolin, *Sensors*, 2008, **8**, 6015–6025.

17 B. J. Yakes, R. J. Lipert, J. P. Bannantine and M. D. Porter, *Clin. Vaccine Immunol.*, 2008, **15**, 227–234.

18 S. Ding, C. Mosher, X. Y. Lee, S. R. Das, A. A. Cargill, X. Tang, B. Chen, E. S. McLamore, C. Gomes, J. M. Hostetter and J. C. Claussen, *ACS Sensors*, 2017, **2**, 210–217.

19 D. Farrell, R. G. Shaughnessy, L. Britton, D. E. MacHugh, B. Markey and S. V. Gordon, *PLoS One*, 2015, **10**, e0134310.

20 R. G. Shaughnessy, D. Farrell, K. Riepema, D. Bakker and S. V. Gordon, *PLoS One*, 2015, **10**, e0145089.

21 M. Malvisi, F. Palazzo, N. Morandi, B. Lazzari, J. L. Williams, G. Pagnacco and G. Minozzi, *PLoS One*, 2016, **11**, e0164461.

22 T. Kilic, A. Erdem, M. Ozsoz and S. Carrara, *Biosens. Bioelectron.*, 2018, **99**, 525–546.

23 C. Ye, M. Q. Wang, L. J. Li, H. Q. Luo and N. B. Li, *Nanoscale*, 2017, **9**, 7526–7532.

24 C. Y. Song, Y. J. Yang, B. Y. Yang, Y. Z. Sun, Y. P. Zhao and L. H. Wang, *Nanoscale*, 2016, **8**, 17365–17373.

25 R. Chand and S. Neethirajan, *Biosens. Bioelectron.*, 2017, **98**, 47–53.

26 M. B. Gawande, A. Goswami, F. X. Felpin, T. Asefa, X. Huang, R. Silva, X. Zou, R. Zboril and R. S. Varma, *Chem. Rev.*, 2016, **116**, 3722–3811.

27 J. Liu and Y. Lu, *Nat. Protoc.*, 2006, **1**, 246–252.

28 J. N. Coleman, M. Lotya, A. O'Neill, S. D. Bergin, P. J. King, U. Khan, K. Young, A. Gaucher, S. De, R. J. Smith, I. V. Shvets, S. K. Arora, G. Stanton, H.-Y. Kim, K. Lee, G. T. Kim, G. S. Duesberg, T. Hallam, J. J. Boland, J. J. Wang, J. F. Donegan, J. C. Grunlan, G. Moriarty, A. Shmeliov, R. J. Nicholls, J. M. Perkins, E. M. Grieveson, K. Theuwissen, D. W. McComb, P. D. Nellist and V. Nicolosi, *Science*, 2011, **331**, 568–571.

View Article Online
DOI: 10.1039/C8NR00697K

29 J. Yu, W. Yin, X. Zheng, G. Tian, X. Zhang, T. Bao, X. Dong, Z. Wang, Z. Gu, X. Ma and Y. Zhao, *Theranostics*, 2015, **5**, 931–945.

30 J. Wang, Q. Deng, M. Li, K. Jiang, J. Zhang, Z. Hu and J. Chu, *Sci. Rep.*, 2017, **7**, 8903.

View Article Online
DOI: 10.1039/C8NR00697K

Table 1. Multiplex detection of miRNAs in spiked serum

miRNAs (pM)	Expected signal (μA)	Signal obtained (μA)				Average % error
		$miRNA_{205}$	$miRNA_{92}$	$miRNA_{7857}$	$miRNA_{378}$	
1000	41.33	42.17	42.68	42.57	42.35	2.69
750	29.4	29.95	30.21	30.36	30.19	2.57
250	18.73	19.77	19.95	19.32	20.13	5.62

View Article Online
DOI: 10.1039/C8NR00697K

Table 2. . Performance of pTb miRNAs sesnsor evaluated using bovine samples

Sample	ELISA	RT-PCR	Electrochemical detection (This work)			
			$miRNA_{205}$	$miRNA_{92}$	$miRNA_{7857}$	$miRNA_{378}$
1	P	P	N	P	P	P
2	P	P	P	N	P	N
3	P	P	P	P	P	P
4	P	p	P	P	N	P
5	P	P	P	N	P	P

View Article Online
DOI: 10.1039/C8NR00697K

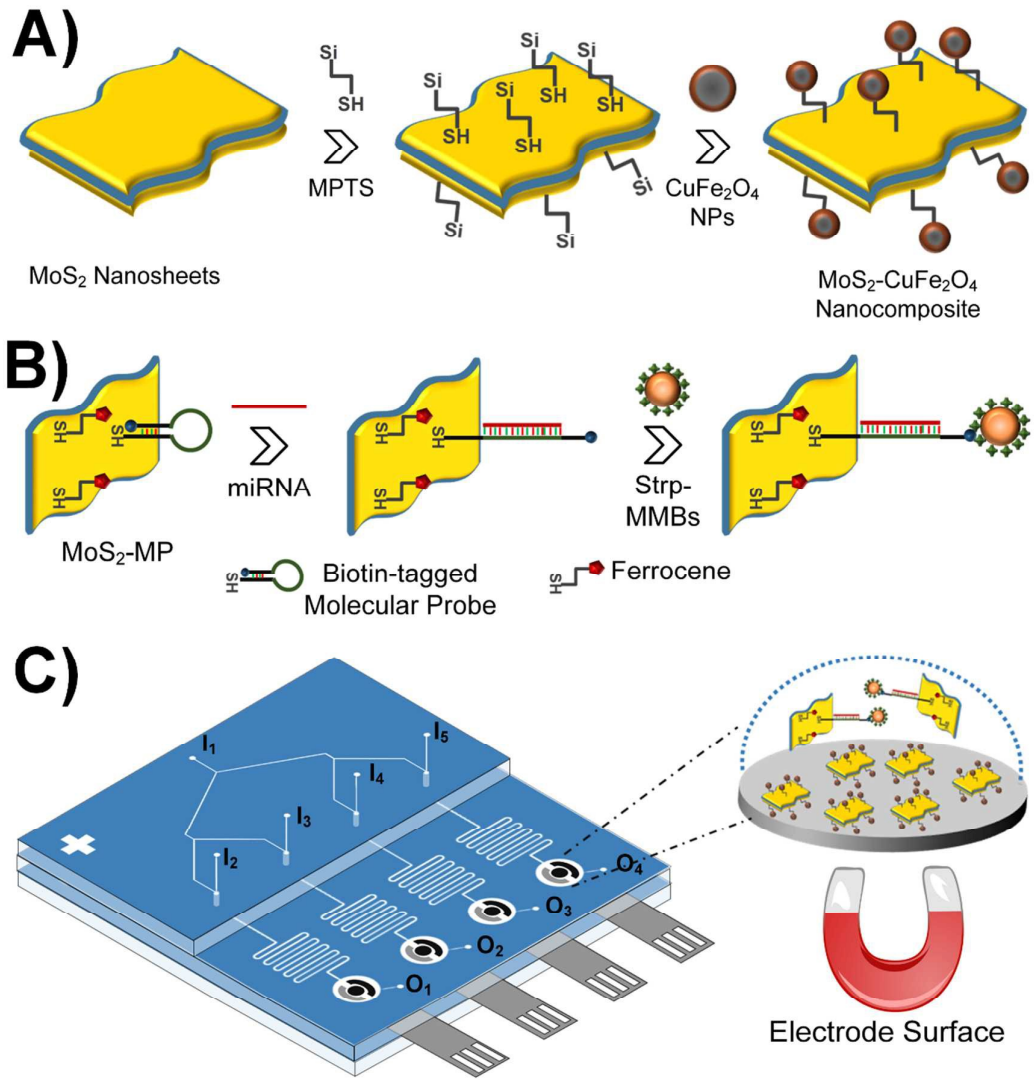

Figure 1. MoS_2 nanosheets based electrochemical miRNAs sensor: A) Schematic of MoS_2-$CuFe_2O_4$ nanocomposites synthesis, B) Principle of miRNAs detection using MoS_2-MP nanocarriers, and C) Structure of PDMS microfluidic platform showing inlets (I_{1-5}), mixing zones, incubation zones, sensing zones, outlets (O_{1-4}) and integrated electrodes, inset: miRNA detection on nanocomposites modified electrode.

View Article Online
DOI: 10.1039/C8NR00697K

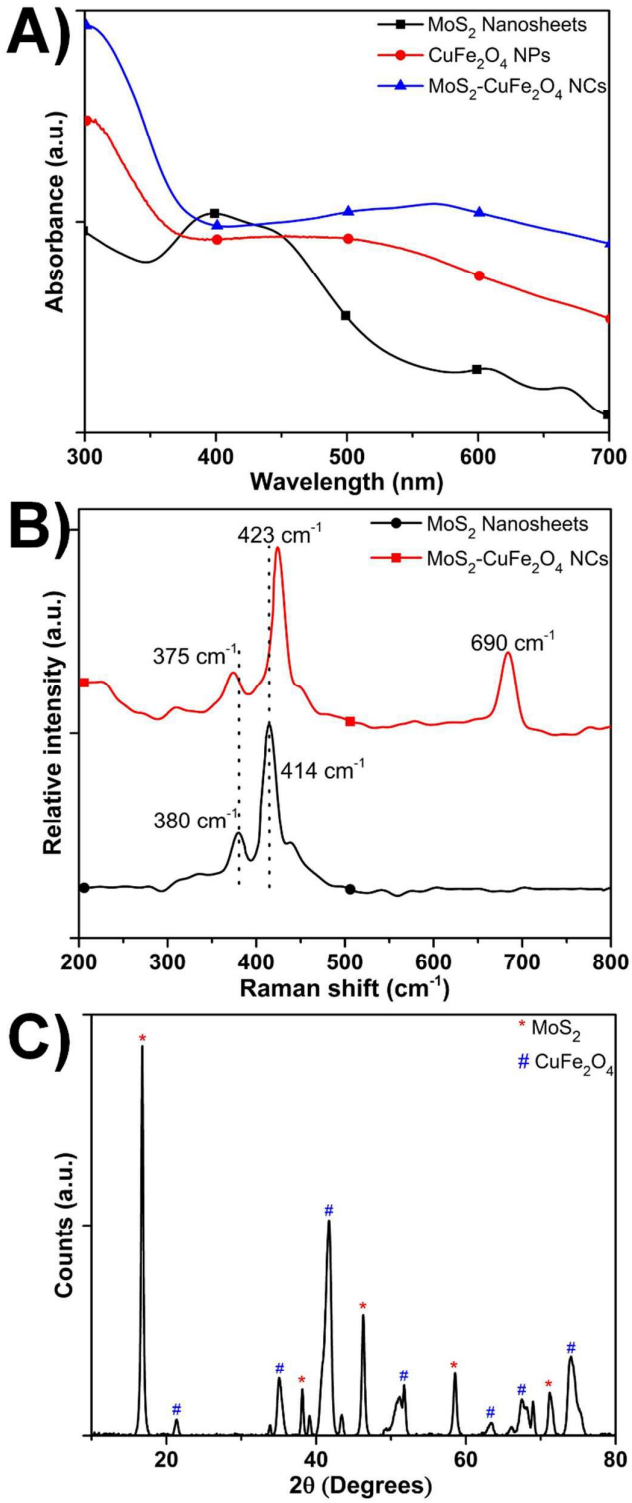

Figure 2. Characterization of MoS_2-$CuFe_2O_4$ nanocomposites: A) UV–visible spectroscopy, (B) Raman spectra, and C) XRD spectra.

View Article Online
DOI: 10.1039/C8NR00697K

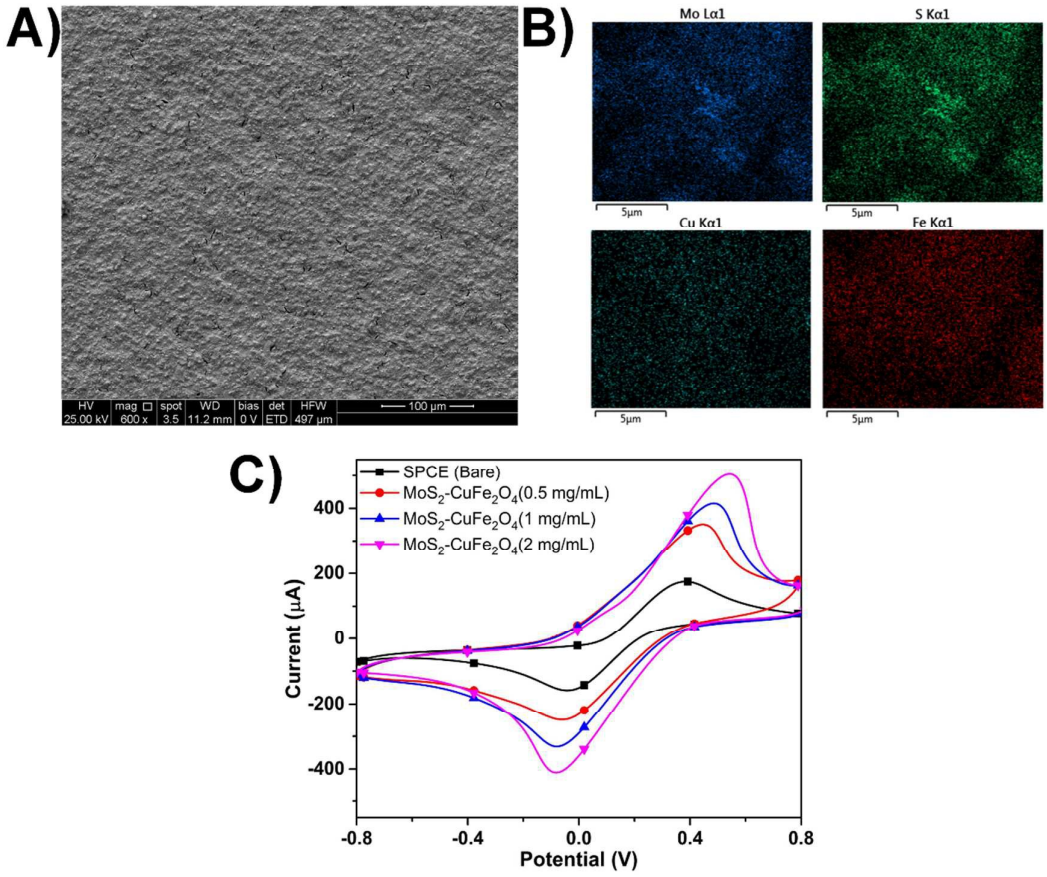

Figure 3. Characterization of MoS_2-$CuFe_2O_4$ nanocomposites modified electrode: A) SEM image, B) Elemental mapping showing Mo, S, Cu, and Fe, and C) CVs of 5 mM $[Fe(CN)_6]^{3-/4-}$ after different nanocomposites electro-polymerization, Buffer: 1X PBS, Scan rate: 100 mV/sec.

View Article Online
DOI: 10.1039/C8NR00697K

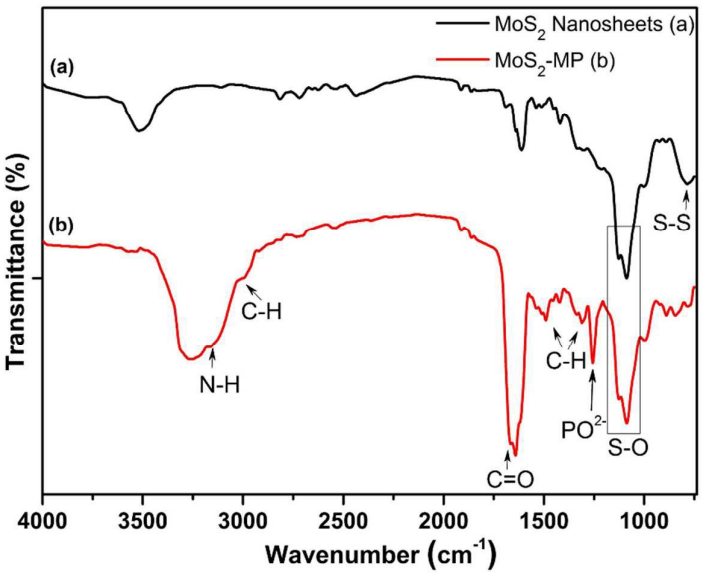

Figure 4. FTIR spectra of MoS_2 nanosheets and MoS_2−MP nanocarriers.

View Article Online
DOI: 10.1039/C8NR00697K

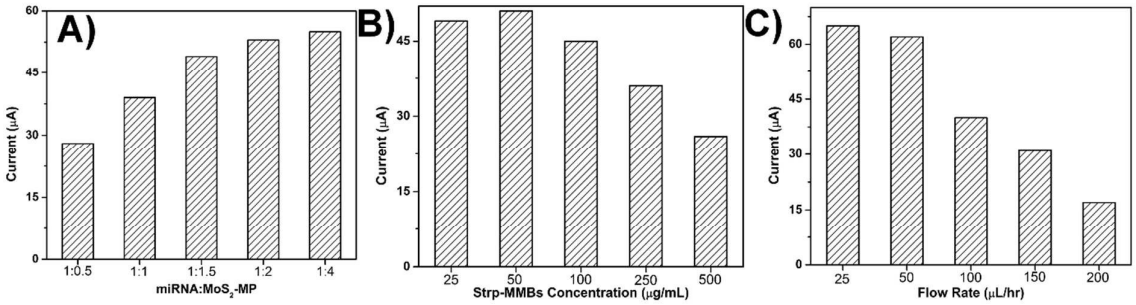

Figure 5. Optimization of miRNA (1.5 nM) sensing: (A) MoS_2-MP concentration, with Strp-MMBs = 100 μg/mL and incubation time = 2 hrs; (B) Strp-MMBs concentration, with miRNA:MoS_2-MP = 1:2 and incubation time = 2 hrs; C) Flow rate of sample and nanocarriers with miRNA:MoS_2-MP = 1:2 and Strp-MMBs = 50 μg/mL.

View Article Online
DOI: 10.1039/C8NR00697K

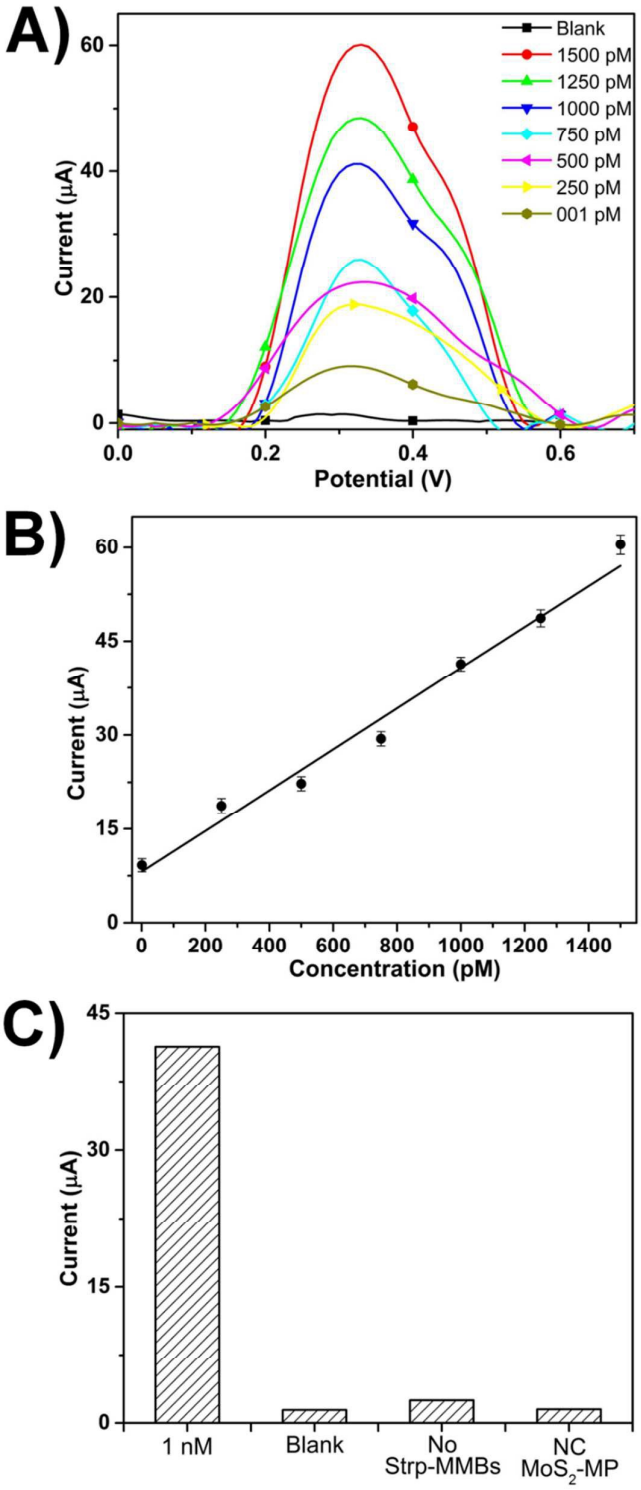

Figure 6. Microfluidic electrochemical sensing of $miRNA_{205}$: (A) SWVs of various concentrations of miRNA, Buffer: 1X PBS, (B) Calibration curve of miRNA sensing derived from the SWVs, R^2=0.97, Error bars= standard deviation (n=3), C) Response of miRNA

View Article Online
DOI: 10.1039/C8NR00697K

sensor in the absence of Strp-MMBs and in presence of non-complementary (NC) molecular probe.

View Article Online
DOI: 10.1039/C8NR00697K

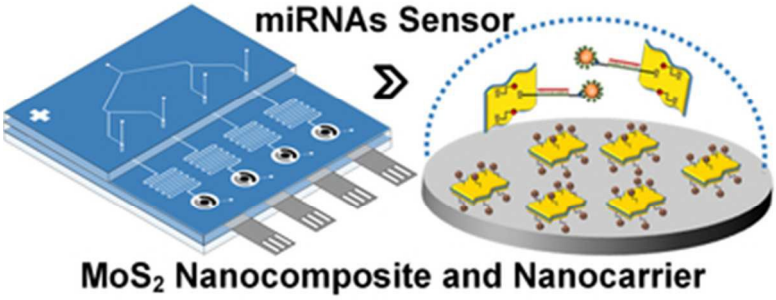

32x13mm (300 x 300 DPI)